

## Space telescopes

PHILIPPE LEMAIRE<sup>I</sup>, BERND ASCHENBACH<sup>II</sup> AND JOHN F. SEELY<sup>III</sup>

### Abstract

A brief survey of normal and grazing incidence space telescope types is given. The optimization of telescope efficiency either by dedicated single, bi-layer or multi-layer coatings is described. An outlook of solar and stellar coronagraphs is included.

### Introduction

Telescopes for astronomical observations have been in use for four centuries by now. Even for telescopes used in space which covers a much shorter time period it is not possible to give a detailed and complete description in a few pages, although the optical characteristics of the normal-incidence space (NI) telescopes are derived from ground-based telescopes. In this article, the most important parameters are recalled but for more details and complementary information see books on optics, such as *Astronomical Optics* (Schroeder 2000).

The choice and specification of the optically relevant parameters of each individual telescope are related to the scientific objectives and the constraints imposed by the celestial object under study and/or the capacity of the spacecraft in terms of mass, volume and electrical power which eventually can be supplied.

To fully design a telescope appropriate to the scientific objectives the following topics should be considered and weighed against each other:

- stellar observations (point-like sources), imagery or/and spectroscopy,
- interstellar medium and/or galaxy observations in wide-field mode (extended sources),
- solar observations, imagery or/and spectroscopy,
- spectral range or wavelength domain and efficiency,
- angular resolution and field of view (FOV),
- spacecraft parameters (size and mass allocations, pointing system performance, choice of spacecraft orbit,...),
- acceptable level of scattered light and baffling requirements.

---

<sup>I</sup>IAS—Institut d’Astrophysique Spatiale, Paris, France

<sup>II</sup>MPE—Max-Planck-Institut für extraterrestrische Physik, Garching, Germany

<sup>III</sup>SSD/NRL—Space Science Division, Naval Research Laboratory, Washington DC, USA

## Report Documentation Page

*Form Approved*  
*OMB No. 0704-0188*

Public reporting burden for the collection of information is estimated to average 1 hour per response, including the time for reviewing instructions, searching existing data sources, gathering and maintaining the data needed, and completing and reviewing the collection of information. Send comments regarding this burden estimate or any other aspect of this collection of information, including suggestions for reducing this burden, to Washington Headquarters Services, Directorate for Information Operations and Reports, 1215 Jefferson Davis Highway, Suite 1204, Arlington VA 22202-4302. Respondents should be aware that notwithstanding any other provision of law, no person shall be subject to a penalty for failing to comply with a collection of information if it does not display a currently valid OMB control number.

1. REPORT DATE <b>2010</b>	2. REPORT TYPE	3. DATES COVERED <b>00-00-2010 to 00-00-2010</b>			
4. TITLE AND SUBTITLE <b>Space telescopes</b>		5a. CONTRACT NUMBER			
		5b. GRANT NUMBER			
		5c. PROGRAM ELEMENT NUMBER			
6. AUTHOR(S)		5d. PROJECT NUMBER			
		5e. TASK NUMBER			
		5f. WORK UNIT NUMBER			
7. PERFORMING ORGANIZATION NAME(S) AND ADDRESS(ES) <b>Institut d'Astrophysique Spatiale, Paris, France, , ,</b>		8. PERFORMING ORGANIZATION REPORT NUMBER			
9. SPONSORING/MONITORING AGENCY NAME(S) AND ADDRESS(ES)		10. SPONSOR/MONITOR'S ACRONYM(S)			
		11. SPONSOR/MONITOR'S REPORT NUMBER(S)			
12. DISTRIBUTION/AVAILABILITY STATEMENT <b>Approved for public release; distribution unlimited</b>					
13. SUPPLEMENTARY NOTES <b>Chapter title ?Space telescopes? , by Lemaire, Philippe; Aschenbach, Bernd; Seely, John F. (Third author is from NRL)In: Observing Photons in Space by M.C.E. Huber, A. Pauluhn, J.L. Culhane, J.G. Timothy, K. Wilhelm, and A. Zehnder (eds.). ISSI (International Space Science Institute, Bern, Switzerland,) Scientific Reports Series, ESA/ISSI. ISBN 978-92-9221-938-8, 2010, p. 165-191.</b>					
14. ABSTRACT <b>A brief survey of normal and grazing incidence space telescope types is given. The optimization of telescope efficiency either by dedicated single, bi-layer or multilayer coatings is described. An outlook of solar and stellar coronagraphs is included.</b>					
15. SUBJECT TERMS					
16. SECURITY CLASSIFICATION OF:			17. LIMITATION OF ABSTRACT	18. NUMBER OF PAGES	19a. NAME OF RESPONSIBLE PERSON
a. REPORT <b>unclassified</b>	b. ABSTRACT <b>unclassified</b>	c. THIS PAGE <b>unclassified</b>	<b>Public Release</b>	<b>27</b>	

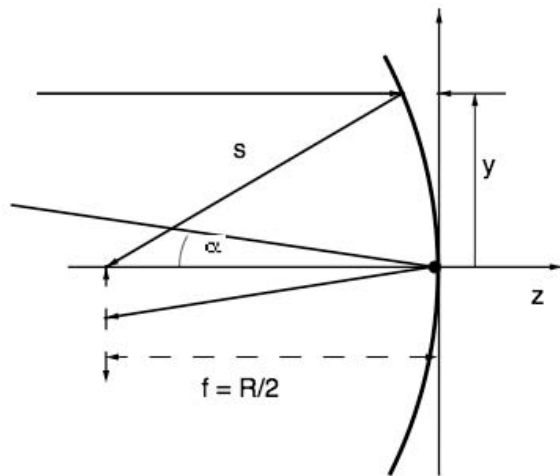


Figure 9.1: Paraboloid telescope.

In the following sections, NI reflective telescopes are considered for use only if the mirror coating reflectivity (single or multilayer) permits efficient observations. At shorter wavelengths, i.e., shorter than about 70 nm (EUV), grazing-incidence (GI) telescopes could be considered as an alternative. At even shorter wavelengths, i.e., shorter than about 5 nm up to hard X-rays with photon energies up to about 100 keV, GI telescopes are the only choice. To increase the mirror reflectivity both for NI and for GI mirrors, multilayer coatings have successfully been developed. A special case of telescopes are the coronagraphs, which have been in use for more than fifty years of observing the solar corona and which are now being developed to observe very faint stars or planets nearby a brighter star.

## Normal-incidence telescopes

### One-mirror telescope

The one-mirror telescope (mostly an off-axis paraboloid; Figure 9.1) has been developed to feed spectrometers in the VUV wavelength range where the use of only one reflecting surface provides better efficiency. It also offers a high-resolution instantaneous small field of view (FOV). The image is being scanned while maintaining the paraboloid's image quality, which can be achieved by either a rotation of the mirror around its vertex in case of a small field, or by rotation around its focus for a large field, or by rotation of the whole instrument (see SUMER/*SOHO*, Wilhelm et al (1995) and EIS/*Hinode*, Culhane et al (2007)). The paraboloid field curvature (Petzval surface) is  $k_p = 2/R$ , where  $R$  is the paraboloid radius.

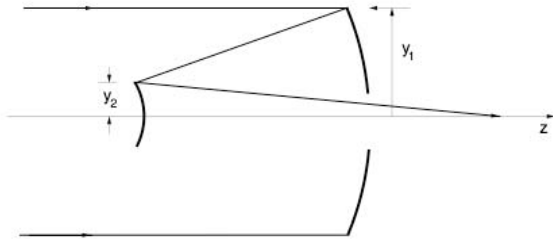


Figure 9.2: Cassegrain telescope.

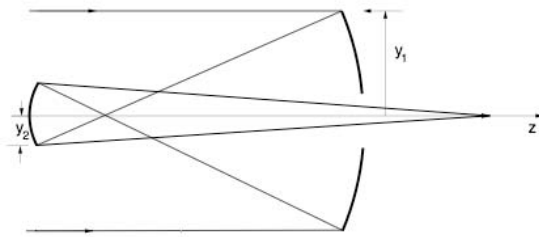


Figure 9.3: Gregorian telescope.

## Two-mirror telescopes

Telescopes employing two mirrors are used to feed spectrometers or to make imagery (through wavelength filters) with small or/and wide FOV from the near-infrared to the extreme-ultraviolet wavelength range. A high-quality image over a small field is provided by a Cassegrain-type telescope—a compact telescope, Figure 9.2, e.g., *Copernicus* (Rogerson et al 1973), LPSP (Artzner et al 1977) and LASP (Bruner 1977) on *OSO-8*—or by a Gregorian-type telescope with intermediate primary focus that can be used as field stop, Figure 9.3, e.g., HRTS/*Spacelab 2* (Brueckner et al 1986), SOT/*Hinode* (Shimizu 2004). A high-quality image over a large field (up to  $1^\circ$ ) can be obtained by a Ritchey–Chrétien-type telescope, e.g., *IUE* (Boggess et al 1977), *HST* (Jenkner 1990) and EIT/*SOHO* (Delaboudinière et al 1995). Small-field pointing can be controlled by actuating the secondary mirror while large-offset pointing is done with the full-telescope pointing. The Petzval curvature is given by  $k_p = 2((1 - \rho)/\rho)/R_1$  where  $\rho = R_2/R_1$ . For a Gregorian telescope  $\rho$  is less than zero and the Petzval surface is convex as seen from the secondary mirror, while for a Cassegrain telescope the Petzval surface is concave.

## Telescope parameters

The characteristic parameters of the telescopes for the most frequently used combinations of two mirrors are described in Table 9.1, where  $m_s$  is the secondary

Table 9.1: Telescope characteristics.

$m_s$	$k_h$	$\rho$	Type	Secondary
$> 1$	$> 0$	$> 0$	Cassegrain	convex
$= 1$	$> 0$	$\infty$	Cassegrain	flat
0 to 1	$> 0$	$< 0$	Cassegrain	concave
$< 0$	$< 0$	$< 0$	Gregorian	concave
$< 0$	$> 1$	$> 0$	inverse Cassegrain	concave

magnification,  $k_h$  is the ratio of heights at mirror margins and  $\rho$  is the ratio of mirror radius of curvature. The relations between the parameters are:

$$m_s = \frac{\rho}{(\rho - k_h)}, \quad \rho = \frac{m_s k_h}{(m_s - 1)}, \quad k_h = \frac{(1 + \beta)}{(m_s + 1)}, \quad (9.1)$$

where  $\beta$  is the back focal distance in units of  $f_1$  (primary mirror focal length). If  $K$  is the conic constant, the classical type telescope (Cassegrain or Gregorian) has

$$K_1 = -1, \quad K_2 = - \left[ \frac{(m_s + 1)}{(m_s - 1)} \right]^2, \quad (9.2)$$

whereas the aplanatic type telescope (Ritchey–Chrétien) has

$$K_1 = -1 - \frac{2(1 + \beta)}{m_s^2(m_s - \beta)}, \quad K_2 = - \left( \frac{m_s + 1}{m_s - 1} \right)^2 - \frac{2m_s(m_s + 1)}{(m_s - \beta)(m_s - 1)^3}. \quad (9.3)$$

## Point-spread function and relative encircled energy

The image quality of a perfect telescope with circular aperture is given by the point-spread function (PSF) which provides the image extension in one direction. The normalized PSF is expressed by the following equation:

$$\frac{I_\nu}{I_0} = \frac{1}{(1 - \epsilon^2)^2} \left[ \frac{2J_1(\nu)}{\nu} - \epsilon^2 \frac{2J_1(\epsilon\nu)}{\epsilon\nu} \right]^2. \quad (9.4)$$

Another way to qualify the image is the relative encircled energy (EE) which gives the energy distribution within a point image. The relative EE is obtained through the equation:

$$\begin{aligned} E_E(\nu_0) &= \frac{1}{1 - \epsilon^2} \left[ 1 - J_0^2(\nu_0) - J_1^2(\nu_0) + \epsilon^2 (1 - J_0^2(\epsilon\nu_0) - J_1^2(\epsilon\nu_0)) \right] \\ &\quad - \frac{2\epsilon}{1 - \epsilon^2} \left[ \int_0^{\nu_0} J_1(\epsilon\nu) \frac{2J_1(\nu)}{\nu} d\nu \right], \end{aligned} \quad (9.5)$$

where  $\epsilon$  is the obscuration ratio (ratio of secondary to primary mirror diameters) and  $\nu/\pi = (2/\lambda)(a/R)r$ , with  $a$  the radius of the main mirror,  $R$  the radius of

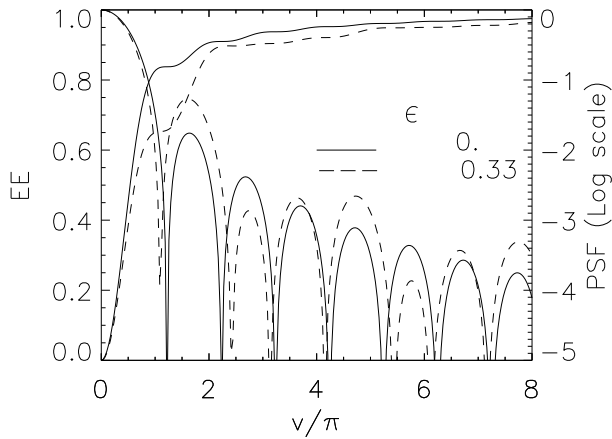


Figure 9.4: PSF (lines undulating along abscissa) and EE (lines increasing monotonically along abscissa) for a perfect image with obscuration factor  $\epsilon$  of 0 and 0.33.

curvature of the main mirror,  $r$  the distance from the focal point in the image plane.  $J_0$  and  $J_1$  are the Bessel functions of zero and first orders. Figure 9.4 gives the variations of the PSF and EE with  $\epsilon = 0$  (off-axis single or two-mirror telescope) and  $\epsilon = 0.33$  (the obscuration of the *HST*).

## Classical aberrations for a centred pupil

The classical and other aberrations are treated in detail by Schroeder (2000). A summary is given in the following subsections.

### Paraboloid telescope

The transverse sagittal coma ( $C_{ST}$ ), the transverse astigmatism ( $A_{ST}$ ), the angular astigmatism ( $A_{SA}$ ) and the angular sagittal coma ( $C_{SA}$ ) are given by the relations:

$$C_{ST} = -\frac{y^2}{R^2} \theta s, \quad A_{ST} = -\frac{2y}{R} \theta^2 s, \quad C_{SA} = \frac{\theta}{16F^2}, \quad A_{SA} = \frac{\theta^2}{2F}, \quad (9.6)$$

where  $F$  is the system focal ratio ( $f/D$ , telescope focal length over its aperture diameter),  $R$  is the system radius ( $2f$ ),  $y$  is the ray height at mirror margin,  $\theta$  is the angular field and  $s = f$  on the telescope axis (focal distance, otherwise it is the distance between the mirror vertex and the focus).

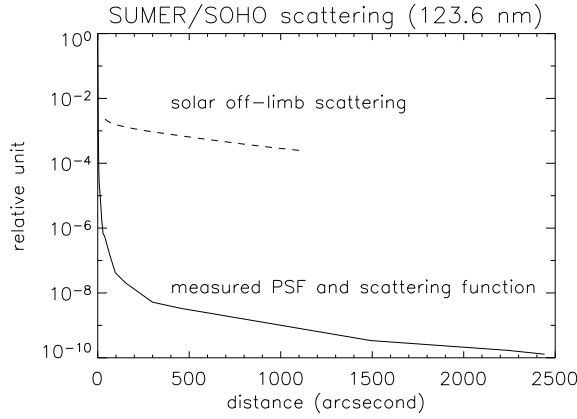


Figure 9.5: SUMER telescope scattering. The solid line gives the measured extension of the PSF combined with the scattering function (Saha and Leviton 1993) and the dotted line the computed and measured solar (32' diameter) off-limb scattering.

### Two-mirror telescope (Cassegrain or Gregorian)

For the classical two-mirror telescope the  $C_{SA}$  and  $A_{SA}$  aberrations and the angular distortion ( $D_{IA}$ ) are defined as:

$$\begin{aligned} C_{SA} &= \frac{\theta}{16 F^2}, \quad A_{SA} = \frac{\theta^2}{2 F} \frac{m_s^2 + \beta}{m_s(1 + \beta)}, \\ D_{IA} &= \frac{\theta^3(m_s - \beta)(m_s^2 - 1)(m_s + 3\beta)}{4 m_s^2(1 + \beta)^2}, \end{aligned} \quad (9.7)$$

where  $m_s$  and  $\beta$  have been defined in previous sections.

### Aplanetic two-mirror telescope (Ritchey–Chrétien)

In the case of the aplanetic (no spherical aberration and no coma) two-mirror telescope the modified  $A_{SA}$  and  $D_{IA}$  aberrations are:

$$\begin{aligned} A_{SA} &= \frac{\theta^2}{2 F} \frac{m_s(2 m_s + 1) + \beta}{2 m_s(1 + \beta)}, \\ D_{IA} &= \frac{\theta^3(m_s - \beta)[m_s(m_s^2 - 2) + \beta(3 m_s^2 - 2)]}{4 m_s^2(1 + \beta)^2}. \end{aligned} \quad (9.8)$$

### Mirror scattering

Optical surface mirror irregularities with spatial mid-frequency errors (roughness) and spatial high-frequency errors (micro-roughness) give rise to wavelength

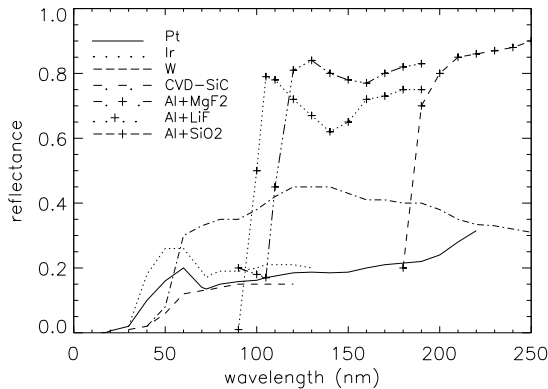


Figure 9.6: Reflectance of several coatings in the VUV at near NI.

dependent angularly scattered light. The dimmed specular reflection  $I_r$  is given by the relation:

$$I_r/I_0 = \exp[-(4\pi\sigma \cos \alpha/\lambda)^2] \quad , \quad (9.9)$$

where  $I_0$  is the reflection of the mirror with perfect surface,  $\sigma$  is the root mean square (RMS) of the residual surface errors,  $\alpha$  is the incidence angle and  $\lambda$  the wavelength. One aspect of the mirror scattering is the redistribution of light far from the specular image in the focal plane, cf., the one-mirror telescope scattering of SUMER in Figure 9.5 (Saha and Leviton 1993). For a point source such as a star, a bright star can mask a weak star or a planet; for extended sources, nearby features (the corona in case of the Sun or weak emitters for nebulae and galaxies) can be left undetectable.

## Loss of image quality

Multiple factors can modify the image quality:

- mirror surface deformations by mechanical and/or thermal constraints (the choice of the mirror blank material and the mounting are critical for space application),
- alignment errors (secondary misalignment: tilt or decentre, despace (Schroeder 2000)),
- pointing errors (Schroeder 2000),
- degradation of mirror surfaces and coatings by particulates and/or molecular deposition.

Cleanliness control of the optics and minimizing surface contamination is absolutely essential and critical for VUV and shorter wavelength telescopes (especially under the strong solar UV flux (Lemaire 1991) and/or in the case of coronagraphs).

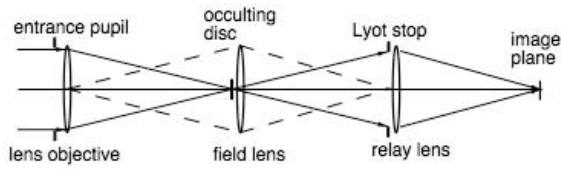


Figure 9.7: The Lyot solar coronagraph scheme.

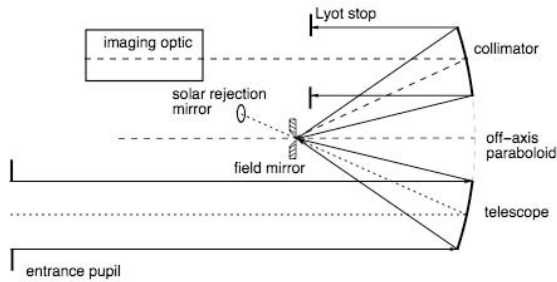


Figure 9.8: Solar reflecting coronagraph C1/LASCO.

## Classical mirror coatings

For most applications, working in several wavelength ranges requires wide-band mirror coatings with high efficiency. In the VUV wavelength range, the coating efficiency strongly varies with wavelength (e.g., Figure 9.6) and the number of reflections must be minimized. The most frequently used coatings for the visible wavelength range are Ag and Al+SiO<sub>2</sub>, but Al+MgF<sub>2</sub> is used to cover the FUV-visible wavelength range. Au is used in the near infrared.

## Coronagraphs

Historically the coronagraph has been developed for solar corona observations. The Lyot coronagraph (Lyot 1932) basic design is shown in Figure 9.7 with a well defined pupil, an occulting disc to mask the image and a Lyot stop (at the pupil image location) to stop the high-intensity diffraction pattern given by the pupil edge. Using the Lyot idea new solar and stellar coronagraphs have been designed.

### Solar coronagraphs

#### Reflecting solar coronagraph

An all-reflecting coronagraph has been designed and operated on *SOHO* (Figure 9.8, Brueckner et al 1995). The telescope part uses an unobstructed off-axis paraboloid.

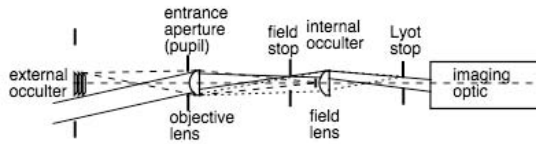


Figure 9.9: Solar refracting coronagraph with external occulter, C2/LASCO.

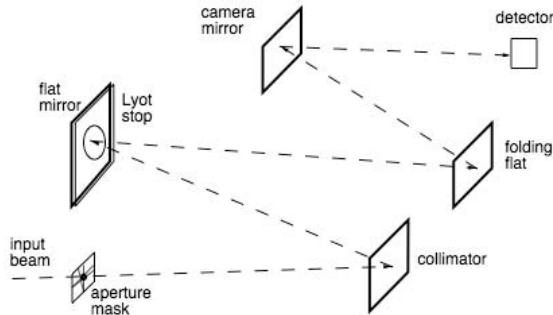


Figure 9.10: Optical scheme of the STIS-*HST* coronagraph (Heap et al 2000).

### Solar coronagraph with external occulter

To observe the corona far away from the solar disk with a radiance ratio of  $L/L_{\text{disk}} \ll 10^{-8}$  an external occulter is used (Figure 9.9) for the C2 and C3 LASCO coronagraphs on *SOHO* (Brueckner et al 1995).

### Stellar coronagraphs

To observe faint objects (stars or planets) nearby a bright object several techniques have been studied and are (or will be) implemented in space instrumentation.

#### Classical Lyot scheme

This technique, derived from the Lyot scheme, has been implemented in the STIS (Space Telescope Imaging Spectrograph) spectrometer (Figure 9.10, Heap et al 2000). An aperture mask stops the specular image of the bright star, and a Lyot stop eliminates the diffraction pattern of the entrance pupil.

#### Other coronagraph designs

The search, detection and analysis of the atmosphere of Earth-like planets in orbit around a bright star require coronagraphs with very low scatter (about  $10^{-10}$  in the visible or  $10^{-7}$  in the near mid-infrared). These numbers are for a separation of  $0.1''$  of the two-component star/planet system located at a distance from the

Earth of 10 pc. A lot of studies are running to search for the optimized design for future missions. Most of them try to combine the advantages of a Lyot design and an interferometric combination of beams, one being  $\pi$ -phase shifted and flipped to obtain a nulling interferometer as suggested by Bracewell (1978). An evaluation of the expected performances of several proposed coronagraphs has been made by Guyon et al (2006).

## Grazing-incidence telescopes

### The physics of GI reflection

One way to focus and image sources of light is by using curved reflecting surfaces. The interaction of light with matter can be described by the complex index of refraction which describes the change of the properties of the incident electromagnetic wave when crossing the boundary between the two materials involved. The index  $n$  reads:

$$n = 1 - \delta - i\beta \quad . \quad (9.10)$$

$\delta$  describes the phase change and  $\beta$  accounts for the absorption. The reflection coefficients for  $p$  and  $s$  polarization are given by the Fresnel equations:

$$r_p = \left( \frac{E_r}{E_i} \right)_p = \frac{n^2 \sin \theta - \sqrt{(n^2 - \cos^2 \theta)}}{n^2 \sin \theta + \sqrt{(n^2 - \cos^2 \theta)}} \quad , \quad (9.11)$$

$$r_s = \left( \frac{E_r}{E_i} \right)_s = \frac{\sin \theta - \sqrt{(n^2 - \cos^2 \theta)}}{\sin \theta + \sqrt{(n^2 - \cos^2 \theta)}} \quad . \quad (9.12)$$

$E_r/E_i$  denotes the ratio of the amplitudes of the reflected and incident electric fields and  $\theta$  is the grazing angle of incidence as measured from the interface plane. For NI, which is the standard in optical telescopes,  $\theta \approx 90^\circ$ . This approach is correct as long as the assumptions for applying the Fresnel equations are fulfilled. The reflected intensity or reflectivity is then  $R_p = r_p \times r_p^*$  and  $R_s = r_s \times r_s^*$ , where the asterisk denotes the conjugate complex value.

The components of the index of refraction for a vacuum/matter transition are often called the optical constants of the material. In the optical wavelength range, for instance, the real part of the index of refraction is greater than one, but with decreasing wavelength it becomes less than one, which changes the interaction of light with matter dramatically. The reflectivity of the surface at NI decreases rapidly and the mirrors lose efficiency starting in the UV wavelength band. However, applying Snell's law to the incident and refracted light, it turns out that the refraction angle measured from the surface normal is greater than  $90^\circ$  for  $n_r = 1 - \delta < 1$ , or that total external reflection occurs for GI angles  $\theta \leq \theta_t$ :

$$\cos \theta_t = 1 - \delta \quad , \quad (9.13)$$

or for  $\delta \ll 1$ :

$$\theta_t = \sqrt{2\delta} \quad . \quad (9.14)$$

For actual applications a trade-off is to be made in terms of the effective collecting area between the designs of a NI telescope or alternatively a GI telescope. The effective collecting area is the product of the wavelength-dependent reflectivity times the geometric area of the primary mirror projected on the front aperture. Depending on the number of the reflecting optical elements involved, GI telescopes tend to be more efficient for wavelengths shorter than about 30 nm. Furthermore the reflectivity at NI drops so rapidly with decreasing wavelength that for observations at wavelengths shorter than about 15 nm GI is the only choice. This limit can be extended somewhat to even shorter wavelengths by the use of multilayer coatings on the mirror but only over a fairly restricted wavelength band. Multilayer coatings of several hundreds of bi-layers, each a couple of 0.1 nm thick, can also be applied to GI mirrors, thereby extending the photon energy range out to about 100 keV.

The index of refraction or the optical constants can be computed from anomalous dispersion theory. For wavelengths  $\lambda$  or photon energies sufficiently offset from any electron binding energy, a coarse estimate of  $\delta$  can be made:

$$\delta = \frac{r_e}{2\pi} \frac{N_A \rho}{A} Z \lambda^2 \quad , \quad (9.15)$$

where  $N_A$  is Avogadro's number,  $r_e$  is the classical electron radius,  $Z$  and  $A$  are the atomic number and weight, respectively, and  $\rho$  is the mass density. For heavy elements for which  $Z/A \approx 0.5$ , the incidence angle of total reflection for  $\delta \ll 1$  can be estimated to:

$$\theta_t = 5.6' \frac{\lambda}{0.1 \text{ nm}} \sqrt{\frac{\rho}{\text{g cm}^{-3}}} \quad . \quad (9.16)$$

For X-rays, with  $\lambda$  of a few 0.1 nm,  $\theta_t$  is about  $1^\circ$ . Equation 9.16 suggests the most dense materials are most suitable for reflective coatings, such as gold, platinum or iridium, which have all been used for X-ray space telescope mirrors. However, these materials show a pronounced reduction of reflectivity at energies between 2 keV and 4 keV, because of the presence of M-shell absorption, so that nickel, for instance, despite its lower density has sometimes been preferred, in particular for observations below 4 keV.

The optical constants are related to the atomic scattering factors, the most up-to-date tables of which have been compiled by the Center for X-ray Optics (Henke et al 1993).<sup>1</sup> These tables cover the energy range from 50 eV to 30 keV for the elements with  $Z = 1$  to 92, and are a very useful data basis for designing GI optics.

## GI telescope configurations

At GI imaging of an extended source or imaging over some extended field requires at least two reflections, i.e., two reflecting surfaces. Single mirrors like GI parabolas suffer from strong coma preventing true imaging. However, such a mirror can still focus and parabolas have been used as 'light buckets'.

There are three different configurations of two-mirror systems which are the Wolter-type systems, the Kirkpatrick-Baez type systems and the focussing collimator or 'lobster-eye' systems.

<sup>1</sup>[http://henke.lbl.gov/optical\\_constants/](http://henke.lbl.gov/optical_constants/)

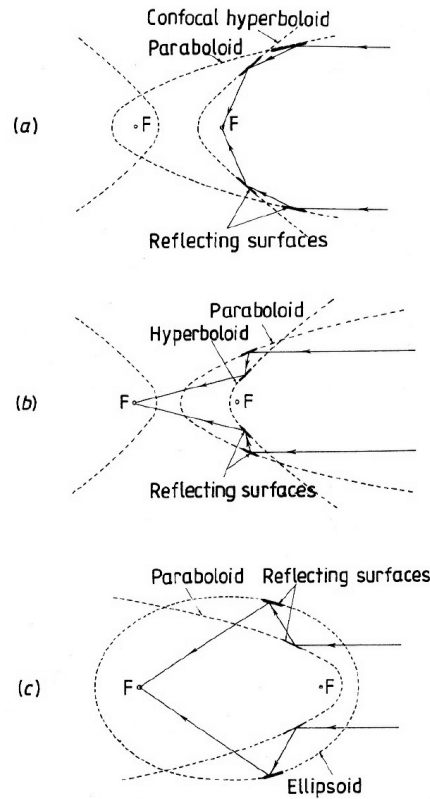


Figure 9.11: Schematic of Wolter telescopes (a) Type I, (b) Type II and (c) Type III.

### Wolter telescopes

In 1952, Hans Wolter suggested three different types of imaging telescopes for GI (cf., Figure 9.11), which have become known as Wolter telescopes of Type I, Type II and Type III (Wolter 1952a). The surfaces used encompass a paraboloid, a hyperboloid and an ellipsoid. Type I and Type II make use of a paraboloid and a hyperboloid, type III combines a paraboloid and an ellipsoid. In each case the two mirrors involved are arranged in a coaxial and confocal manner. The main difference between the three types is the ratio of focal length to total system length, i.e., the minimum physical length of the telescope. The focal length of a Type I system is practically given by the distance from the paraboloid/hyperboloid intersection plane to the system focus. Therefore the physical telescope length always exceeds the focal length by the length of the paraboloid. This system has been mostly used in space observations because of its compactness, simple configuration as far as the interface to the mounting structure is concerned, and because it provides free space to easily add further telescopes inside and outside. These telescopes with

multiple components are called nested systems. They increase the collecting area substantially.

Single Type I systems have been used for solar X-ray observations, whereas for astronomical EUV and X-ray observations, for which collecting area is of utmost importance, nested systems have been used, cf., the *Einstein* observatory (Van Speybroeck 1979; Giacconi et al 1979) *EXOSAT* (de Korte et al 1981), *ROSAT* (Aschenbach 1988), *ASCA* (Serlemitsos et al 1995) and *Suzaku* (Serlemitsos et al 2007), *Chandra* (Van Speybroeck 1988; Van Speybroeck et al 1997), and *XMM-Newton* (Aschenbach et al 2000), as well as the JET-X telescope of the *Swift* mission (Citterio et al 1996; Burrows et al 2005). For instance, each of the three X-ray telescopes on board of *XMM-Newton* (Aschenbach et al 2000) accommodates 58 nested paraboloid-hyperboloid Wolter Type I mirror shell pairs.

The Wolter Type II system is a true telescopic system, for which the focal length can be much longer than the physical length of the telescope. These systems are useful for feeding spectrometers which require large dispersion.

Wolter-type systems are free of spherical aberration, but still suffer from coma aberration, astigmatism and field curvature. In a second paper Wolter presented the equations for grazing telescopes which exactly obey the Abbe sine condition, which eliminates coma. This is achieved by very small corrections (sub-micrometre to 1  $\mu\text{m}$ ) of the axial mirror profile from its nominal second-order shape. The exact surface shape has been derived by Wolter by extending the solutions to GI that Schwarzschild had already obtained for NI in 1905 (Schwarzschild 1905). Therefore, these systems are named Wolter–Schwarzschild telescopes (Wolter 1952b). They supersede the Wolter systems in off-axis imaging performance if used at longer wavelengths, i.e., in the EUV and the soft X-ray band. Wolter–Schwarzschild Type I telescopes were flown on the *EUV-Explorer* (Bowyer and Green 1988; Bowyer and Malina 1991) and the *ROSAT-WFC* (Willingale 1988). A Wolter–Schwarzschild Type II system fed the spectroscopic telescope of the *EUV-Explorer*, and the CDS telescope on board of *SOHO* (Harrison et al 1995) is of the Wolter–Schwarzschild Type II.

The maximum degree of nesting, and therefore the highest throughput relative to the entrance aperture area, is achieved with mirrors as thin as possible. Hundreds of thin foils or sheets representing the mirrors make up the telescopes used in the *ASCA* and *Suzaku* missions. The parabolic/hyperbolic shape of the Wolter Type I mirrors is approximated by straight cones. The perfect image of an on-axis point source is lost but the imaging capability is preserved. Cone approximation of the Wolter Type I configuration has also been used for the *BeppoSAX* X-ray telescopes (Citterio et al 1986).

### Kirkpatrick–Baez telescopes

The first two-dimensional X-ray image ever obtained with GI reflection was taken in the laboratory by Kirkpatrick and Baez (1948). The telescope configuration is shown in Figure 9.12. The incident rays are focused to a line image by a parabolic mirror. On their path to the line focus the rays are reflected by a second parabolic mirror to the point-like focus for rays parallel to the centre lines of the parabolas. The surface planes of the two mirrors are oriented at  $90^\circ$  to each other. In order to

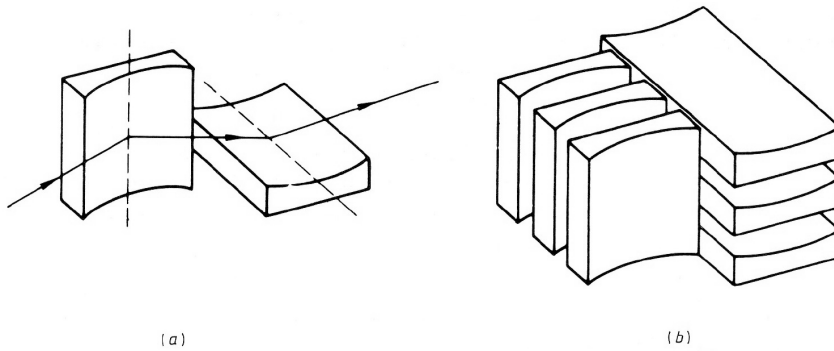


Figure 9.12: Schematic of the Kirkpatrick–Baez telescope. (a) shows a two-mirror combination, (b) displays a stack of several mirrors.

increase the collecting area (the frontal area) a stack of parabolas of translation can be constructed. However, in contrast to the single double-plate system the image of a point-like source starts to become extended, increasing in size with the number of plates involved. Wolter Type I telescopes bend the incident ray direction two times in the same plane, whereas the two bendings in Kirkpatrick–Baez systems occur in two orthogonal planes, which for the same incidence angle on the primary mirror requires a longer telescope.

#### Focussing collimator or ‘lobster-eye’ telescopes

The Wolter and the Kirkpatrick–Baez systems have in common a relatively narrow field of view which is practically limited to the grazing angle employed on the individual mirrors. Imaging systems of substantially larger field of view but at systematically reduced on-axis angular resolution have been proposed by Schmidt (1975) and by Angel (1979). Such systems would be ideal for a wide-field imaging monitor.

The principal layout of Schmidt’s concept is shown in Figure 9.13. Two stacks of plane mirrors form the telescope. The upper as well as the lower stack consist of a series of plane mirrors, reflecting on both sides, in an orthogonal configuration. The mirrors within each stack are arranged in such a way that their centre lines outline a cylinder. The two cylinders are at right angles to each other, and the crossing of their centre lines is at the origin of the coordinate system. A focus is formed half way between the mirrors and the origin of the coordinate system. The focussing is not perfect because of the finite height of the mirror blades. With such a device a full hemisphere of the sky could be observed simultaneously.

A variation of this design, which provides two-dimensional imaging, has been presented by Angel (1979) (see also Priedhorsky et al 1996, and references therein). The device is composed of many small square-sided tubes with reflecting surfaces. The tubes are based and distributed over the surface of a sphere. The axis of each tube follows a radius vector of the sphere. After a ray has been reflected twice

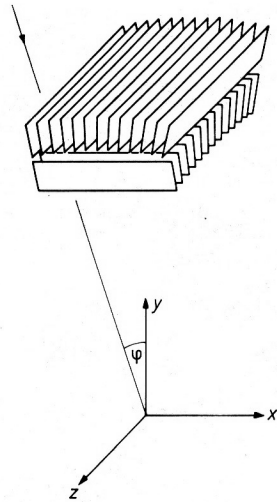


Figure 9.13: Flat-mirror two-dimensional focussing collimator or detached lobster-eye configuration (Schmidt 1975).

within one tube but from adjacent walls a two-dimensional image is formed. The focal surface is a sphere with a radius which is half that of the sphere carrying the tubes. This type of GI optic is actually realized in the reflective eyes of lobsters and shrimps, giving the name to this particular type of X-ray telescope. That the optical principle is very similar to Schmidt's focussing collimator can be seen if the upper and lower mirror stacks of this device are shifted and merged into one section forming square-sided tubes.

Both in the Schmidt and the Angel design there are rays passing through the optics with only one reflection or none at all. They appear as diffuse or line-shaped backgrounds of non-negligible brightness. Per se, the imaging is not perfect, but, ultimately, the angular resolution of such a device is limited by the width of a single tube as seen by the detector, and at second-of-arc resolution the diffraction imposed by the tube width has to be observed, favouring such a system for observing hard X-rays. Such a telescope would have great potential for continuous X-ray monitoring of large fields of the sky.

## Design considerations

### Parameters

The choice of a particular type of GI telescope depends on the scientific objectives. First of all, the highest photon energy has to be considered, which according to Equation 9.16 defines the optimum grazing angle. Such energies are found, for instance, in the astrophysically important Fe K-lines between 6.4 keV and 7 keV.

The *XMM-Newton* telescope was designed to optimally cover this region and to provide an acceptable area at 2 keV.

Surveying telescopes should have a low  $f$ -number, which is equivalent to maximizing the product of the effective collecting area times the field of view. This requires a grazing angle as large as possible but compatible with the average photon energy within the band to be observed. The *ROSAT* telescope was designed along these lines. Furthermore, such a survey telescope should have the best possible angular resolution over a field of view as wide as possible. Wolter Type I telescopes show strong field curvature, which means that the angular resolution increases rapidly with growing field angle (off-axis angle, Van Speybroeck and Chase 1972). The so-called *polynomial telescopes* tend to flatten the field (Burrows et al 1992; Conconi and Campana 2001). They maintain the Wolter configuration but the second-order surface shape is replaced by higher-order polynomials at the expense of degrading the on-axis resolution. Alternatively, for nested systems, the primary mirrors of a Wolter telescope should be kept as short as possible without compromising the free entrance aperture.

### Effective collecting area

These trade-offs are usually done by detailed ray-tracing taking into account the reflectivity of the coating, which usually changes substantially with energy. Figure 9.14 shows the effective collecting area of one of the three *XMM-Newton* telescopes. The widest of the 58 nested Wolter Type I mirror pairs has a diameter of 70 cm. The geometric area of the entrance aperture is about 3100 cm<sup>2</sup> and the effective area at the lowest energies (cf., Figure 9.14) is about 1850 cm<sup>2</sup>, equivalent to a throughput of less than 60 %. This can be increased by the use of thinner mirrors like foils or thin sheets with which a throughput of more than 80 % has been achieved. The on-axis angular resolution of such foil telescopes, however, is so far limited to about 1'.

### Angular resolution, PSF, EE function

Even for a perfect telescope the light from a point-like object located on-axis is not concentrated in an infinitely small focal spot, but is distributed over an extended image, the surface brightness of which is described by the PSF. The EE function corresponds to the radial integration of the PSF and describes the relative fraction of effective area within some radius. At large field angles the image extent and structure are dominated by geometric aberrations inherent to the telescope design. In contrast, the on-axis PSF is determined by differences between the real and perfect shape of the reflecting surfaces, both in circumferential and in axial direction, as well as by alignment and mounting errors. For high-resolution telescopes, most demanding is the control of the surface shape by appropriate metrology, through which a highly precise feedback to computer controlled grinding and polishing of the relevant surfaces down to residuals of a few 0.1 nm on either the mirrors or mandrels has become possible. Because of GI the tightest requirements have to be observed for surface errors along the mirror meridional or axial profiles. They need to be as low as possible over all spatial frequency scales which

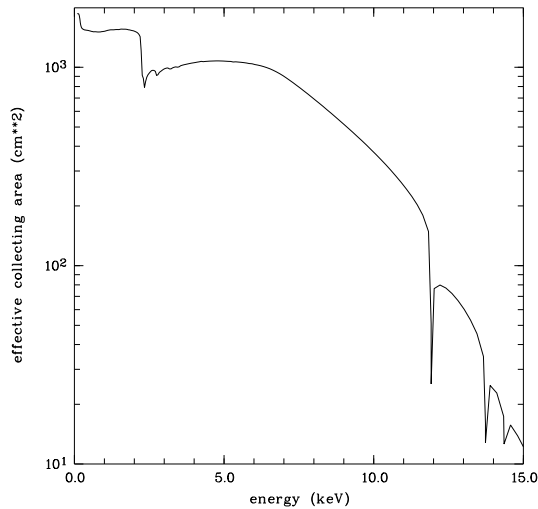


Figure 9.14: On-axis effective collecting area of one of the three *XMM-Newton* X-ray telescopes, as designed. All 58 mirror pairs have been coated with gold, which causes the energy dependence of the area. The jumps and wiggles are due to the binding energies of the N-, M- and L-shell electrons.

range from the full mirror length up to the micrometre range. The same holds for circumferential errors. Low-frequency errors can be considered as geometric slope errors and they can be treated by geometric optics. At high frequencies the errors and their power spectral density distribution can be understood as scattering from randomly rough surfaces (Aschenbach 2005). The fraction  $I_s/I_0$  of scattered X-rays is given by:

$$I_s/I_0 = 1 - \exp[-(4\pi\sigma \sin\theta/\lambda)^2] \quad . \quad (9.17)$$

The micro-roughness  $\sigma$  is the RMS value of the surface height deviations. Micro-roughness reduces the image contrast, produces a loss of flux out of the image core and raises extended wings in the PSF. In the early days of GI mirrors scattering was a major problem because of the low values for  $\sigma$  to be achieved for a reasonable high-contrast image. For instance, for  $I_s/I_0 = 0.1$  at X-ray wavelengths ( $\lambda = 1$  nm) and GI ( $\theta = 1^\circ$ ) a micro-roughness of  $\sigma = 0.9$  nm is required. Values like 0.3 nm have become possible on highly aspherical GI mirrors and have been realised on the *ROSAT* telescope mirrors.

The shape of the PSF core is generated by geometric errors, the total of which accumulates to less than  $0.1''$  for the *Chandra* telescope. Figure 9.15 shows the on-axis EEs for the *Chandra* telescope at various photon energies. Energy-dependent scattering, as expected from Equation 9.17, appears to be present.

## Baffling

GI telescopes have to be equipped with field stops to baffle the focal plane against stray-light. Otherwise rays from outside the nominal field of view can pass through the telescope by a single reflection from either the primary or the secondary.

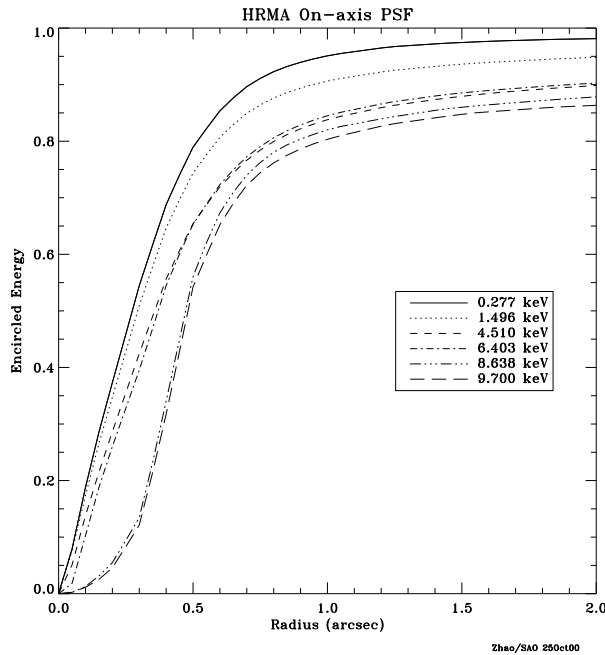


Figure 9.15: EE function of the *Chandra* telescope for different photon energies (Chandra 2003).

There may be even portions of the sky which can be viewed directly from the focal plane detector. Such stray-light increases the background light and produces ghost images. A complete suppression of stray-light requires field stops in several different planes, which are best in front of the telescope aperture and down in the telescope's mirror section. For tightly nested systems with little if any available space between adjacent mirrors a single baffle system in front of the telescope can be used, which, however, reduces but not completely eliminates stray-light.

## Multilayer coatings

For wavelengths less than approximately 50 nm, the NI reflectance of a coating consisting of a single layer diminishes with decreasing wavelength as illustrated in Figure 9.6. While the reflectance can be large for grazing angles smaller than the critical angle of total internal reflection,  $\theta_t \approx \sqrt{2\delta}$ , where  $\delta$  is a parameter related to the real part of the complex index of refraction  $n = 1 - \delta - i\beta$ , the values of  $\delta$  and  $\theta_t$  become small in the X-ray region resulting in small instrument collection angle and low throughput. Multilayer interference coatings can be utilized to greatly increase the EUV NI reflectance and the X-ray reflectance at grazing angles larger than the critical angle. When applied to solar and astrophysical telescope mirrors, high-reflectance multilayer coatings enable high-throughput and high-cadence observations of transient and faint radiation sources. In addition,

the multilayer coating's reflectance profile can be optimized for narrow-waveband imaging and for broad-waveband spectroscopy applications.

The design and fabrication of multilayer interference coatings for the EUV and soft X-ray regions was pioneered by Eberhard Spiller and Troy Barbee. Spiller (1994) wrote an excellent introduction. In this section, we emphasize the utility of multilayers for solar and astrophysical telescopes and for spectrometers and discuss recent developments in the field.

A multilayer interference coating typically consists of alternating layers of two materials with high contrast in the optical constants  $\delta$  and  $\beta$ , where  $1 - \delta$  is the real part of the index of refraction and  $\beta$  is the absorption coefficient. One material has low absorption coefficient and functions as the spacer material, and the other material has relatively high reflectivity and functions as the scattering material. The multilayer coating performs similar to a quarter wave stack, where the electromagnetic waves reflected from the scattering layer interfaces are in phase and constructively interfere when the bilayer thickness  $d$  satisfies the Bragg relation  $2d \sin \theta = m \lambda$  (neglecting small index of refraction corrections). Thus for NI,  $\sin \theta = 1$  and in the first interference order ( $m = 1$ ) the bilayer thickness, the sum of the spacer and scattering layer thicknesses, is equal to half the operating wavelength  $\lambda$ . To a first approximation, the peak of the reflectance profile occurs at the wavelength  $\lambda$  satisfying the Bragg relation, and the width of the reflectance profile is  $\lambda/N$  where  $N$  is the number of bilayers that effectively participate in the coating's reflectance and is strongly dependent on the absorption coefficients  $\beta$  of the spacer and scattering layers.

The multilayer coating's reflectance can be calculated using the Fresnel reflectivity coefficient at each layer interface and accounting for absorption in each layer. The effects of micro-roughness and mixing by interdiffusion of the two materials at the interfaces, which reduce the reflectance, can be modelled by a Debye-Waller factor. In order to achieve high reflectance, it is necessary that the micro-roughness and interdiffusion scale lengths be small compared to the wavelength, and a thin barrier layer can be sometimes used to reduce these scale lengths when the spacer and scattering materials do not form discrete, smooth, and stable interfaces. The accuracy of the calculated reflectance primarily depends on the accuracy of the modelling of the layer interfaces and on the accuracy of the optical constants of the layer materials. The optical constants are tabulated in Center (2007), and the IMD code (Windt 1998) is widely used to calculate multilayer reflectances in the EUV and X-ray regions.

## NI EUV multilayer coatings

For NI multilayers operating in the EUV region, the spacer material is selected to have an absorption edge at a wavelength below the operating wavelength. Then the spacer material is relatively transmissive at the operating wavelength, and a large number of bilayers ( $N$ ) can contribute to the reflectance. The scattering material is selected to have good material compatibility with the spacer material, resulting in discrete and stable interfaces, and to have high contrast in the optical constants, resulting in high reflectivity at the interfaces. One of the most widely used material combinations for NI EUV multilayers is Si and Mo (Barbee et al

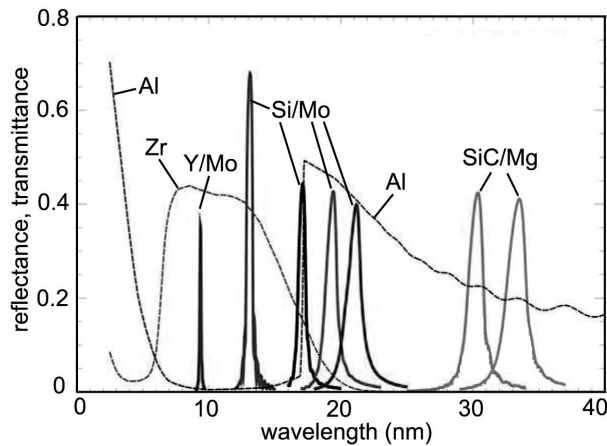


Figure 9.16: Reflectances of the seven AIA multilayer coatings and transmittances of the Al and Zr filters (Soufli et al 2005).

1985). Si is transmissive at wavelengths longer than the Si L edge at 12.42 nm, and Mo has relatively high reflectivity at those wavelengths and has good material compatibility with Si. NI telescopes with highly reflective Si/Mo coatings, or variations, such as Si/Mo<sub>2</sub>C, were utilized on numerous rocket missions and subsequent satellite missions for recording solar images with high spatial resolution such as EIT (Delaboudinière et al 1995) and *TRACE* (Handy et al 1999). The peak of each reflectance profile was tuned to the wavelength of a strong emission line in the solar spectrum by varying the bilayer thickness  $d$ . The value of the peak reflectance and the width of the reflectance profile were optimized by varying the relative layer thicknesses of the spacer and scattering layers.

The next generation of solar imaging telescopes will implement multilayer coatings other than Si/Mo and related coatings for the purposes of narrowing the reflectance profile, increasing the peak reflectance, improving long-term stability, and imaging spectral lines outside the Si/Mo multilayer range (Windt et al 2004). Shown in Figure 9.16 are the reflectances of the seven multilayers planned for the Atmospheric Imaging Assembly (AIA) on *SDO*. AIA will implement a Y/Mo coating at 9.39 nm as well as Si/Mo coatings for four additional wavelengths in the 13.1 nm to 21.1 nm range (Soufli et al 2005). SiC/Mg coatings were planned for 30.4 nm and 33.5 nm and were replaced by SiC/Si for improved stability.

In addition to greatly increasing the sensitivity of EUV NI imaging telescopes, multilayer coatings have also been used to enhance the performance of EUV spectrometers operating at NI. The multilayer coating is applied to the diffraction grating and to the collection mirror (if utilized in the instrument). While a narrow reflectance profile with high peak reflectance is desired for imaging telescopes, providing isolation of a spectral line with a specific emission temperature, a broader reflectance profile giving wider wavelength coverage of a number of spectral lines is usually desired for spectroscopy. The first such orbital spectrometer, the Extreme-Ultraviolet Imaging Spectrometer (EIS) on the *Hinode* spacecraft, used Si/Mo mul-

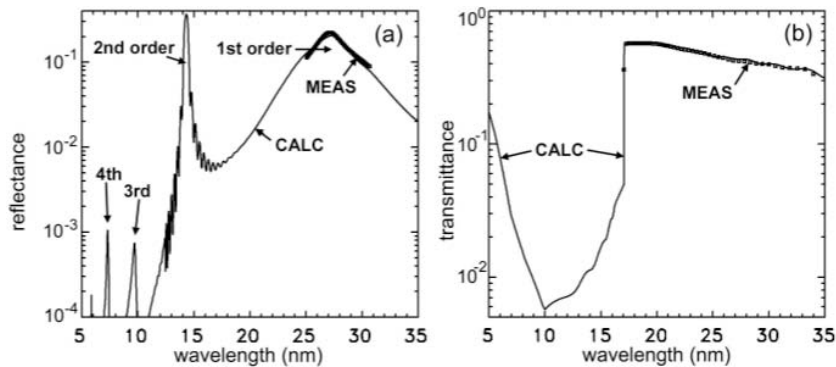


Figure 9.17: (a) Reflectance of the EIS long-band multilayer coatings and (b) transmittance of the EIS aluminum filter.

tilayers on the two halves of a parabolic mirror and a toroidal grating to cover the 17 nm to 21 nm and the 25 nm to 29 nm wavebands (Seely et al 2004).

Multilayer interference coatings can have high reflectance at wavelengths other than the wavelength of the first Bragg order, the usual operating wavelength of EUV imaging telescopes and spectrometers. The reflectance can be large in the higher Bragg orders ( $m > 1$ ) at shorter wavelengths, depending on the optical constants of the multilayer materials. In addition, when the data are recorded by a detector with panchromatic responsivity such as a CCD, the broadband reflectance of UV and visible light from the top layer of the multilayer stack can overwhelm the weaker EUV signal. The out-of-band light is usually blocked by a thin metal filter that transmits the desired EUV radiation and attenuates the shorter wavelengths and the UV and visible light. This is illustrated in Figure 9.17 which shows the reflectance of the EIS long-band (25 nm to 29 nm) multilayer and the transmittance of the 150 nm thick aluminum filter used to block out-of-band radiation. Because of the multilayer design used to optimize the reflectance and bandpass of the coating in the long-band, the Bragg second order at 14.2 nm has higher peak reflectance than the first order at 27 nm; the second order peak is therefore blocked by the filter which has low transmittance below the Al L edge at 17 nm. The higher orders ( $m > 2$ ) have low reflectance owing to absorption in the Si layers at wavelengths shorter than the Si L edge at 12.42 nm.

For multilayer telescopes operating at wavelengths shorter than 17 nm, such as the AIA 9.39 nm and 13.1 nm channels, a zirconium blocking filter can be used as illustrated in Figure 9.16. In general, a multilayer telescope channel operates at a wavelength within a factor of two of the filter absorption edge; otherwise radiation reflected by the multilayer's Bragg second order at half the operating wavelength will be transmitted by the filter and can contaminate the desired Bragg first-order image.

The multilayer reflectances shown in Figure 9.16 indicate that the widths of the reflectance profiles increase with wavelength. This is because fewer bilayers participate in the reflectance owing to increasing absorption with wavelength. The wider reflectance profile can result in contamination of the desired spectral line

signal by neighbouring lines and effectively broadens the temperature of the spectral image. It is possible to reduce the reflectance of neighbouring spectral lines by using an anti-reflection coating on the surface of the multilayer, but this has limited effectiveness and can reduce the reflectance at the desired wavelength at the peak of the reflectance profile. Thus the commonly used multilayers are unsuitable for narrow-waveband imaging for  $\lambda > 35$  nm, and this leads to the search for new multilayer materials. In particular, it is desirable to develop multilayers for narrow-band imaging of the solar O V line at 63.0 nm, which is emitted from solar regions with  $2 \times 10^5$  K temperature, and thereby fills the gap between the low-temperature ( $8 \times 10^4$  K) He II 30.4 nm and the hotter ( $> 10^6$  K) Fe multilayer telescope observations.

Si/Sc multilayers were developed for the 44 nm to 50 nm wavelength range, operating where Sc is relatively transmissive at wavelengths longer than the Sc M edge at 44 nm, and it was found that the stability was improved by adding thin ( $< 1$  nm) W barrier layers between the Si and Sc layers (Vinogradov et al 2001). The development of the Sc based multilayers suggested that other elements with open N and O shells might have transmission windows at wavelengths  $> 50$  nm. However, the lack of accurate optical constants hindered the effort to identify candidate materials (the values of  $\delta$  in the database (Center 2007) extend only to 42 nm). A project was initiated to systematically measure the optical constants of the rare earth (lanthanide) elements that have 4f or 5d open shells (Seely et al 2006). It was found that Tb (Kjornrattanawanich et al 2006) and Gd are relatively transmissive at 63 nm and can be used for narrow-band multilayers.

## GI X-ray multilayer coatings

While NI multilayer coatings have been developed for wavelengths  $< 5$  nm, particularly for the water window range of interest for biological imaging between the O K (2.3 nm) and the C K (4.4 nm) absorption edges, the peak reflectances are typically less than 10 % and are thus far too low for solar and astrophysical instruments. This is primarily the result of interface micro-roughness and interdiffusion with scale lengths that are significant fractions of the operating wavelength and of the layer thicknesses. Mirrors with metal coatings operating at grazing angles smaller than the critical angle have long been used for imaging X-ray wavelengths  $< 1$  nm (photon energies  $> 1.2$  keV). However, the grazing angles decrease with wavelength and result in a small telescope acceptance angle, relatively low throughput, difficulty of alignment, and severe requirements for smooth mirror substrates and coatings.

A periodic (constant  $d$ ) multilayer coating can be designed to have relatively high reflectance at grazing angles larger than the critical angle. However, the reflectance profile is quite narrow in wavelength and in angle owing to the large number of bilayers (typically hundreds or more) participating in the reflectance at short wavelengths where absorption is low. This means that different wavelengths will be reflected along the often long and curved GI mirror, reducing the effective collection area for imaging a specific wavelength. The width of the mirror's reflectance profile can in effect be broadened in wavelength and angle by varying the multilayer period  $d$  along the mirror surface. Broadening can also be achieved

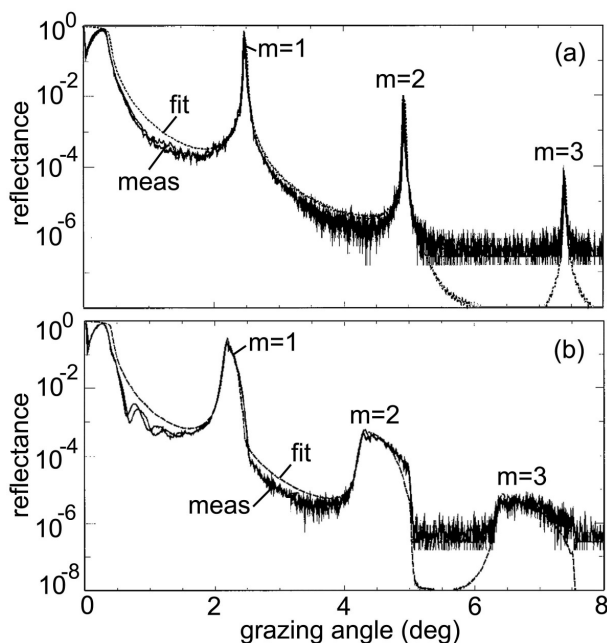


Figure 9.18: Reflectance of (a) periodic W/SiC and (b) depth-graded W/SiC multilayers at 0.154 nm wavelength (Windt et al 2003).

by systematically varying the period with depth into the multilayer, made possible by the large number of bilayers that participate in the reflectance at X-ray wavelengths. In effect, a narrow waveband is reflected by the group of bilayers with thicknesses satisfying the Bragg relation, and a broader range of wavelengths is reflected by properly varying the period laterally or in depth.

Shown in Figure 9.18a is the reflectance of a periodic (constant  $d$ ) W/SiC multilayer as a function of grazing angle measured at 0.154 nm wavelength (8.05 keV Cu K radiation, Windt et al 2003). The multilayer has 300 bilayers with period 1.80 nm. Also indicated is the fit to the measured data using the IMD code and assuming a 0.23 nm interface parameter. This illustrates the narrow Bragg peaks characteristic of a periodic multilayer. For comparison, shown in Figure 9.18b is the GI reflectance of a depth-graded W/SiC multilayer composed of 1100 bilayers, with periods varying from 1.77 nm to 2.10 nm, and the fit to the data indicates an interface parameter equal to 0.26 nm. Compared to the periodic multilayer, the depth-graded multilayer has much broader reflectance orders with smaller peak reflectances.

Shown in Figure 9.19 is the reflectance as a function of photon energy of the depth-graded W/SiC multilayer measured using synchrotron radiation in the 120 keV to 180 keV energy range and at a grazing angle of 2.09 mrad (Windt et al 2003). This illustrates a broad reflectance profile achieved at a relatively large grazing angle; by comparison the critical angle of a single W layer is 0.46 mrad at 160 keV. Also indicated in Figure 9.19 is the fit to the data points using W

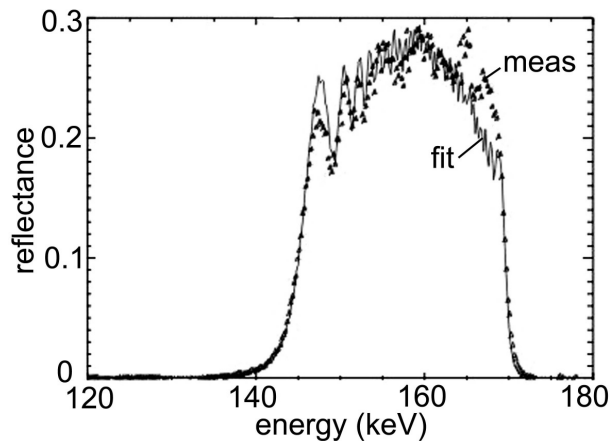


Figure 9.19: Reflectance of a depth-graded W/SiC multilayer measured at 2.09 mrad grazing angle (Windt et al 2003).

and SiC optical constants measured from the reflectance of single W and SiC layers during the multilayer development project. This work demonstrated that it is possible to reliably design and fabricate multilayers, operating at least to 160 keV with a relatively large grazing angle, that are suitable for hard X-ray astrophysical studies.

## Conclusion

Space telescopes have fully taken advantage of ground-based telescope developments. Space extends the observational wavelength range to shortest and longest wavelengths which are not available to ground observations. Dedicated telescopes have been built to take advantage of this extension and a few examples have been reported in this paper. In the future, the progress of space astronomy (as in ground-based astronomy) is related to the ability to observe the finest details and the weakest objects.

## Bibliography

- Angel JRP (1979) Lobster eyes as X-ray telescopes. *Astrophys J* 233:364–373
- Artzner G, Bonnet RM, Lemaire P (plus five authors) (1977) The LPSP instrument on *OSO-8*. I. Instrumentation, description of operations, laboratory calibrations, and pre-launch performance. *Space Sci Instrum* 3:131–161
- Aschenbach B (1988) Design, construction, and performance of the *ROSAT* high-resolution X-ray mirror assembly. *Appl Opt* 27:1404–1413
- Aschenbach B, Briel UG, Haberl F (plus five authors) (2000) Imaging performance of the *XMM-Newton* X-ray telescopes. *Proc SPIE* 4012:731–739

- 
- Aschenbach B (2005) Boundary between geometric and wave optical treatment of X-ray mirrors. *Proc SPIE* 5900:59000D-1–59000D-7
- Barbee TW, Mrowka S, Hettrick MC (1985) Molybdenum-silicon multilayer mirrors for the extreme ultraviolet. *Appl Opt* 24:883–886
- Boggess A, Carr FA, Evans DC (plus 31 authors)(1977) The *IUE* spacecraft and instrumentation. *Nature* 275:372–377
- Bowyer S, Green J (1988) Fabrication, evaluation, and performance of machined metal grazing incidence telescopes. *Appl Opt* 27:1414–1422
- Bowyer S, Malina RF (1991) The extreme ultraviolet explorer mission. *Adv Space Res* 11:205–215
- Bracewell RN (1978) Detecting nonsolar planets by spinning infrared interferometer. *Nature* 274:780–781
- Brueckner GE, Bartoe J-DF, Cook JW (plus two authors) (1986) HRTS results from *Spacelab 2*. *Adv Space Res* 6:263–272
- Brueckner GE, Howard RA, Koomen MJ (plus 12 authors) (1995) The Large Angle Spectroscopic Coronagraph (LASCO). *Sol Phys* 162:357–402
- Bruner EC Jr (1977) The University of Colorado *OSO-8* spectrometer experiment. I: Introduction and optical design considerations. *Space Sci Instrum* 3:369–387
- Burrows CJ, Burg R, Giacconi R. (1992) Optimal grazing incidence optics and its application to wide-field X-ray imaging. *Astrophys J* 392:760–765
- Burrows DN, Hill JE, Nousek JA. (plus 21 authors) (2005) The *Swift* X-ray telescope. *Space Sci Rev* 120:165–195
- Center for X-ray optics. (<http://www-cxro.lbl.gov/>)
- Citterio O, Conti G, Mattaini E (plus two authors) (1986) Optics for X-ray concentrators on board of the astronomy satellite *SAX*. *Proc SPIE* 597:102–110
- Citterio O, Campano S, Conconi, P (plus 11 authors) (1996) Characteristics of the flight model optics for the *JET-X* telescope on board the *Spectrum-X-Gamma* satellite. *Proc SPIE* 2805:56–65
- Conconi P, Campana S (2001) Optimization of grazing incidence mirrors and its application to surveying X-ray telescopes. *Astron Astrophys* 372:1088–1094
- Culhane JL, Harra LK, James AM (plus 36 authors) (2007) The EUV imaging spectrometer for *Hinode*. *Sol Phys* 243:19–61
- Delaboudinière J-P, Artzner GE, Brunaud J (plus 25 authors) (1995) EIT: Extreme-ultraviolet Imaging Telescope for the *SOHO* mission. *Sol Phys* 162:291–312
- Gardner JP, Mather JC, Clampin M (plus 20 authors) (2006) The James Webb Space Telescope. *Space Sci Rev* 123:485–606
- Giacconi R, Branduardi G, Briel U (plus 28 authors) (1979) The *Einstein/HEAO 2/X-ray* Observatory. *Astrophys J* 230:540–550
- Guyon O, Pluzhnik EA, Kuchner MJ (plus two authors) (2006) Theoretical limits on extrasolar terrestrial planet detection with coronagraphs. *Astrophys J Suppl Ser* 167:81–99
- Handy BN, Acton LW, Kankelborg CC (plus 45 authors) (1999) The transition region and coronal explorer. *Sol Phys* 187:229–260
- Harrison RA, Sawyer EC, Carter MK (plus 36 authors) (1995) The Coronal Diagnostic Spectrometer for the Solar and Heliospheric Observatory. *Sol Phys* 162:233–290

- Heap SR, Lindler DJ, Lanz TM (plus five authors) (2000) Space Telescope Imaging Spectrograph coronagraphic observations of  $\beta$  Pictoris. *Astrophys J* 539:435–444
- Henke BL, Gullikson EM, Davis JC (1993) X-Ray interactions: Photoabsorption, scattering, transmission, and reflection at  $E = 50 - 30\,000$  eV,  $Z = 1 - 92$ . *Atomic Data and Nuclear Data Tables* 54(2):181–342
- Jenkner H (1990) The Hubble Space Telescope before launch: A personal perspective. *Rev Mod Astron* 3:297–312
- Kirkpatrick P, Baez AV (1948) Formation of optical images by X-rays. *J Opt Soc Am* 38:766–774
- Kjornrattanawanich B, Windt DL, Seely JF, Uspenskii YuA (2006) SiC/Tb and Si/Tb multilayer coatings for extreme ultraviolet solar imaging. *Appl Opt* 45:1765–1772
- de Korte PAJ, Giralt R, Coste JN (plus four authors) (1981) *EXOSAT* X-ray imaging optics. *Appl Opt* 20:1080–1088
- Lemaire P (1991) Sensitivity changes in the CNRS ultraviolet spectrometer aboard *OSO-8*. *ESA Journal* 15:237–242
- Liyot B (1932) Etude de la couronne solaire en dehors des éclipses. *Z Astrophys* 5:73–95
- Priedhorsky WC, Peele AG, Nugent KA (1996) An X-ray all-sky monitor with extraordinary sensitivity. *Mon Not R Astron Soc* 279:733–750
- Chandra Proposers' Observatory Guide, Rev.6.0, TD 403.00.006 pp. 36–38 (2003)
- Rogerson JB, Spitzer L, Drake JF (plus four authors) (1973) Spectrophotometric results from the *Copernicus* satellite. I. Instrumentation and performance. *Astrophys J* 181:L97–L102
- Saha TT, Leviton DB (1993) Theoretical and measured encircled energy and wide angle scatter of SUMER demonstration telescope mirror in FUV. *Proc SPIE* 1945:398–409
- Schmidt WKH (1975) A proposed X-ray focusing device with wide field of view for use in X-ray astronomy. *Nucl Instr Meth* 127:285–292
- Schroeder DJ (2000) *Astronomical optics*. Academic Press, San Diego, London
- Schwarzschild K (1905) *Untersuchungen zur geometrischen Optik II*, *Abh Wiss Göttingen Bd IV Nr 2*
- Seely JF, Brown CM, Windt DL (plus two authors) (2004) Normal-incidence efficiencies of multilayer-coated laminar gratings for the extreme-ultraviolet imaging spectrometer on the *Solar-B* mission. *Appl Opt* 43:1463–1471
- Seely JF, Uspenskii YuA, Kjornrattanawanich B, Windt DL (2006) Coated photodiode technique for the determination of the optical constants for reactive elements: La and Tb. *Proc SPIE Proc* 6317:OT1–OT9
- Serlemitsos PJ, Jahota L, Soong Y (plus 14 authors) (1995) The X-ray telescope on board *ASCA*. *Pub Astron Soc Jap* 47:105–114
- Serlemitsos PJ, Soong Y, Chan K-W (plus 31 authors) (2007) The X-ray telescope on board *Suzaku*. *Pub Astron Soc Jap* 59:9–21
- Shimizu T (2004) *Solar-B* solar optical telescope (SOT). *ASP Conf Ser* 325:3–14
- Souffi R, Windt DL, Robinson JC (plus eight authors) (2005) Development and testing of EUV multilayer coatings for the atmospheric imaging assembly instrument aboard the Solar Dynamic Observatory. *Proc SPIE* 5901:173–183
- Spiller E (1994) *Soft X-ray optics*. SPIE Press Book, Vol PM15

- 
- Van Speybroeck LP, Chase RC (1972) Design parameters of paraboloid-hyperboloid telescopes for X-ray astronomy. *Appl Opt* 11:440–445
- Van Speybroeck LP (1979) *Einstein* Observatory/*HEAO-B* mirror design and performance. *Proc SPIE* 184:2–10
- Van Speybroeck LP (1988) Grazing incidence optics for the U.S. high-resolution X-ray astronomy program. *Appl Opt* 27:1398–1403
- Van Speybroeck LP, Jerius D, Edgar RJ (plus three authors) (1997) Performance expectation versus reality. *Proc SPIE* 3113:89–104
- Vinogradov AV, Pershin YuP, Zubarev EN (plus six authors) (2001) Structure, thermal stability and reflectivity of Sc/Si and Sc/W/Si/W multilayer X-ray mirrors. *Proc SPIE* 4505:230–235
- Wilhelm K, Curdt W, Marsch E (plus 13 authors) (1995) SUMER – Solar Ultraviolet Measurements of Emitted Radiation. *Sol Phys* 162:189–231
- Willingale R (1988) *ROSAT* wide field camera mirrors. *Appl Opt* 27:1423–1429
- Windt DL (1998) IMD–software for modeling the optical properties of multilayer films. *Comput Phys* 12:360–370
- Windt DL, Donguy S, Hailey CJ (plus seven authors) (2003) W/SiC X-ray multilayers optimized for use above 100 keV. *Appl Opt* 42:2415–2421
- Windt DL, Donguy S, Seely J, Kjornrattanawanich B (2004) Experimental comparison of extreme-ultraviolet multilayers for solar physics. *Appl Opt* 43:1835–1848
- Wolter H (1952a) Spiegelsysteme streifenden Einfalls als abbildende Optiken für Röntgenstrahlen. *Ann Phys (Leipzig)* 445:94–114
- Wolter H (1952b) Verallgemeinerte Schwarzschildsche Spiegelsysteme streifender Reflexion als Optiken für Röntgenstrahlen. *Ann Phys (Leipzig)* 445:286–295